Networked proteins redundantly interact with VAP27 and RABG3 to regulate membrane tethering at the vacuole and beyond

Sabrina Kaiser[1], Dietmar Mehlhorn[2], Paulina Ramirez Miranda[1], Fabian Ries[3], Frederik Sommer[4], Michael Schroda[4], Karin Schumacher[5], Felix Willmund[3], Christopher Grefen[2] and David Scheuring[1,*]

[1] Plant Pathology, University of Kaiserslautern-Landau, Germany
[2] Molecular and Cellular Botany, Ruhr University Bochum, Germany
[3] Molecular Plant Physiology, University of Marburg, Germany
[4] Molecular Biotechnology & Systems Biology, University of Kaiserslautern-Landau, Germany
[5] COS Heidelberg, University of Heidelberg, Germany

*Correspondence: scheuring@bio.uni-kl.de

Abstract

Biological processes in eukaryotes depend on the spatio-temporal compartmentalization of their cells. Integrity and positioning of organelles on the other hand rely on the organization of the actin cytoskeleton. Previously, it has been shown that changes of the plants largest organelle, the vacuole, depend on a functional actin organization. The connection between actin filaments and the vacuole is established by the family of Networked (NET) 4 proteins and, consequently, altering NET4 abundance impacts vacuolar morphology. However, the precise regulatory mechanism is unknown and gene deletions of *NET4* did not result in a global growth phenotype. Here, we show that NET4 functions redundantly with NET3, interacting with RABG3-GTPases at the vacuole to allow for homotypic fusion or, alternatively, the generation of endoplasmic reticulum (ER) - vacuole contact sites. We found that ER-resident NET3 is able to interact with RABG3 residing at the tonoplast and that NET4 interacts with the contact site protein VAP27-1 at the ER. Generation of *net3 net4* triple mutants by CRSIPR-guided mutagenesis helped us to overcome functional redundancy, resulting in impaired plant growth and development. Our results demonstrate how diversification of *NET* genes led to functional redundancy between different family members to create cellular plasticity of vascular plants. We hypothesize that establishment of a direct ER-vacuole connection enables direct lipid and protein transfer which is especially important in young and fast-growing cells. Availability of lipids would facilitate rapidly expanding vacuoles, which are the basis for high cell elongation rates and eventually fast plant growth.

Introduction

Compartmentalization of cells is a hallmark of all eukaryotes. Despite their chemical, physical and structural integrity, organelles need to communicate and exchange material. To this end, all compartments of the endomembrane system are connected via vesicle transport and in addition form membrane contact sites between compartments. Protein transport requires sorting into vesicles via coat proteins, interaction with GTPases, tethering and eventual SNARE (soluble N-ethylmaleimide-sensitive factor attachment receptor)-meditated fusion with the target membrane. In order to target proteins to the lytic vacuole, different trafficking routes can be used (Cui et al., 2020). The best studied transport pathway towards the vacuole includes the sequential recruitment of Rab5-like and Rab7-like GTPases which act as molecular switches, having an inactive GDP-bound and an active GTP-bound state (Ebine et al., 2014). Notably, Rab7-like proteins, called RABGs in plants; have been shown to interact with the HOPS (HOMOTYPIC FUSION AND VACUOLE PROTEIN SORTING) tethering complex at the vacuole (Takemoto et al., 2018). Impairment of any of the HOPS subunits has severe consequences ranging from male sterility (Brillada et al., 2018) to embryo lethality (Rojo et al., 2001), and induced genetic interference results in dramatic fragmentation of the vacuole (Takemoto et al., 2018; Brillada et al., 2018). Together with the CORVET (CLASS C CORE VACUOLE/ENDOSOME TETHERING) complex, the HOPS tethering complex mediates the initial contact between two membranes, thereby regulating vacuolar trafficking (Aniento et al., 2022). Both complexes share a core, consisting of VPS16, VPS18, VPS11, and VPS33 with HOPS having additionally the two specific subunits VPS39 and VPS41. Based on cryo-electron microscopy, the high-resolution structure of the HOPS complex was recently revealed in yeast (Shvarev et al., 2022). Here, SNARE attachment to the core of the hexameric complex is shown and Rab-GTPase binding occurs at the extremities. This represents ideal positioning of molecules to tether two membranes and catalyse their simultaneous fusion (Shvarev et al., 2022).

The formation of membrane contact sites on the other hand involves generally the cytoskeleton, functional and regulatory proteins as well as tethering complexes (Scorrano et al., 2019). The inability of closely associated membranes to fuse, defines membrane contact sites and might be explained by the lack of fusion-competent SNARE complexes. In yeast and animals, numerous contact sites between different organelles have been characterized, most often involving the endoplasmic reticulum (Scorrano et al., 2019). Notably, the formation of contact sites between the ER and lysosomes in animal cells has been reported recently (Tan and Finkel, 2022). Investigations on membrane contact sites in plants came only recently into focus, but in most of the reported cases the ER plays a central role like in animals (Wang et al., 2023). The best studied membrane contact sites in plants are ER-

plasma membrane contact sites (EPCS), whose formation involves a complex interplay of actin filaments, actin-recruiting proteins, microtubules and integral ER proteins (Wang et al., 2014; Zang et al., 2021). The formation of membrane contact sites including plant specific compartments, however, has not been proven unequivocally.

In plants, members of the Networked (NET) family possess actin-binding capacity, localize to different compartments and have been shown to participate in membrane contact site formation (Duckney et al., 2022). Actin filaments and microtubules represent the molecular tracks for moving organelles and molecules within a cell (Vale, 2003). While in animals microtubules are responsible for vesicle trafficking and organelle organization, in plants predominantly actin filaments maintain these functions (Kost and Chua, 2002). The connection between the actin cytoskeleton and the vacuole is mediated by NET4A (Deeks et al., 2012; Kaiser et al., 2019) and misexpression of NET4 impacts size and structure of the vacuole. Whereas a *net4a net4b* double mutant showed more spherical and slightly larger vacuoles, overexpression of *NET4A* (NET4A-GFP^{OE}) rendered vacuoles more spherical but smaller and more condensed around the nucleus (Kaiser et al., 2019). Intriguingly, the appearance of small vacuoles was accompanied by restricted cell elongation and root length similar to what has been previously shown for auxin-induced smaller vacuoles (Scheuring et al., 2016). It seems plausible that limiting vacuole size, regardless of the underlying molecular mechanism, generally inhibits cellular elongation and eventually root growth (Kaiser et al., 2021). It is, however, unclear how NET4 abundancy impacts on the organization of the cytoskeleton and which other molecular players are involved in changing vacuolar morphology. Additionally, gene deletions of *NET4* did not result in a general growth phenotype and we hence expect functional redundancy provided by other proteins.

Here, we show that recruitment of actin filaments by NET4 regulates vacuole fusion, thus providing the driving force to change vacuolar morphology and size. Moreover, NET3 and NET4 proteins redundantly form complexes with RABG3-GTPases, VAP27-1 and actin filaments to establish ER-vacuole membrane contact sites, providing a high level of cellular plasticity. Higher-order *net3 net4* knockout mutants display abnormally shaped and sometimes partially fragmented vacuoles occupying less cellular space. This is accompanied by restricted growth and development, demonstrating that the NET3-NET4 tandem is essential for the development of higher plants.

Results

NET4A abundance changes actin architecture in root cells

The precise regulatory mechanism of changing vacuolar morphology is not yet fully understood and gene deletions of NET4A and NET4B did not result in a general growth phenotype. Previously, we have shown that overexpression of NET4A led to smaller and more compact vacuoles (Kaiser et al., 2019). We could observe the same effect when overexpressing NET4B (Supplementary Fig S1A-E). Since both proteins not only localize to the tonoplast (Kaiser et al., 2019; Supplementary Fig S1F) but also possess a plant specific actin-binding domain (NAB), we expected a reorganization of the cytoskeleton in case of overexpression. To test how NET4 abundance impacts actin architecture, we crossed NET4A-GFP^{OE} with the actin marker lifeact-RFP (Riedl et al., 2008) and quantified changes of filament organization in epidermis cells of the Arabidopsis root tip. Using z-stack recordings, we found a NET4-dependent reorientation of actin filaments towards the cell center, i.e. the nucleus (Fig 1A and 1B). For quantification, we measured parallelness of actin filaments using the LPixel Inc. plugins for ImageJ (https://lpixel.net/en/products/lpixel-imagej-plugins/) according to Higaki (Higaki, 2017), and detected significant differences in actin organization (Fig 1C). This was especially prominent in cells of the transition zone, where central optical sections reveal focusing of actin bundles from the cell periphery towards the nucleus. Accordingly, an impact on vacuole shape could be observed in that area (Supplementary Fig S2). Notably, NET4 signals seem to be pronounced here and colocalize well with the actin marker lifeact-RFP (Fig 1D).

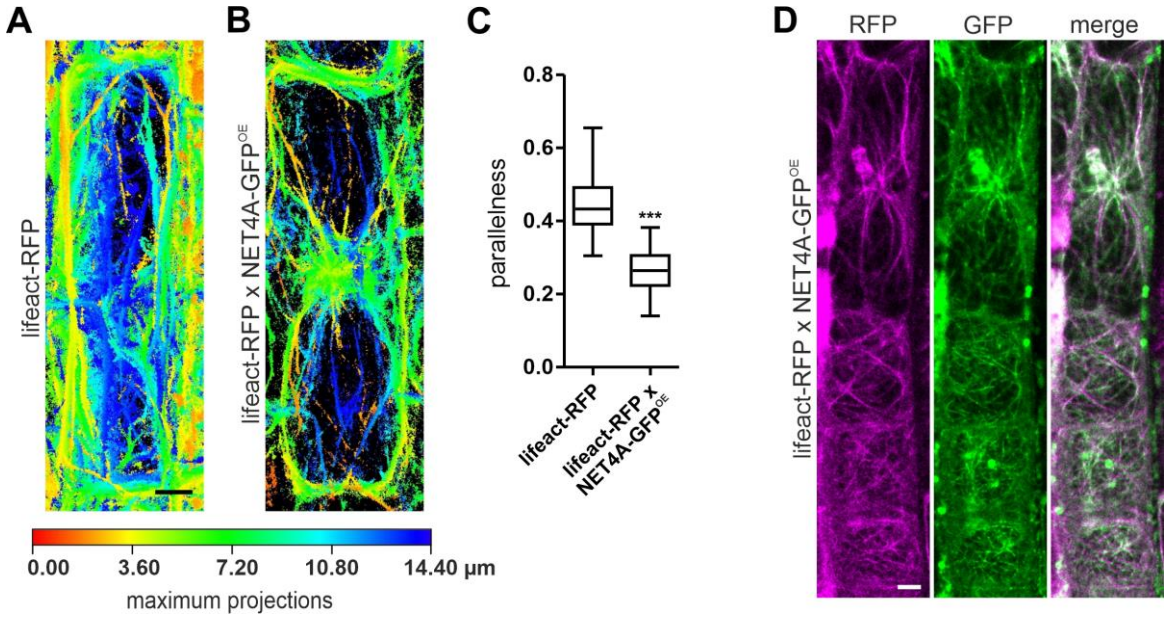

Figure 1 NET4 overexpression changes organization of the actin cytoskeleton. A and B, Maximum projections (depth coded) of actin filaments highlighted by lifeact-RFP for a representative epidermal cell from the transition zone of the Arabidopsis root. A, Control conditions; B, Effect of NET4A overexpression on actin filament organization. C, Quantification of parallelness for the actin cytoskeleton in lifeact-RFP (n=18) and lifeact-RFP x NET4A-GFP^{OE} (n=24). Box limits in the graph represent 25th-75th percentile, the horizontal line the median and whiskers minimum to maximum

values. Significant differences were analyzed by Student's t-test; ***$P < 0.001$. D, Colocalization of NET4A-GFP (green) and lifeact-RFP (magenta). Scale bars in all pictures = 5 µm.

Phenotypes of actin mutants are reverted by *NET4A* overexpression

We hypothesized that overexpression of NET4A led to increased recruitment of actin filaments. To test this, we investigated the effect of NET4A overexpression in different actin-myosin mutant backgrounds. On the subcellular level, we observed that the previously reported more compact vacuoles of the overexpressor line (Kaiser et al., 2019) were more wild type (wt) -like in the *xi-k/1/2* myosin triple mutant (Fig 2A). This effect was more pronounced when the phytohormone auxin (NAA), inducing vacuolar constrictions and further retraction of the tonoplast away from the plasma membrane (Kaiser et al., 2019; Scheuring et al., 2016) was exogenously applied (Fig 2B). To confirm that these changes were indeed caused by NET4A, we crossed the previously described *net4a net4b* double mutant (Kaiser et al., 2019) with NET4A-GFP^{OE}. In the complementation line, both, vacuolar morphology and distance to the plasma membrane (PM), reverted to wt-like appearance (Supplementary Fig S3). When NET4A was overexpressed in the *act7-4* background, the normally irregular cellular organization of the mutant in the root meristem was recovered and cell wall defects were fewer (Fig 2C). Recovery of the *act7-4* mutant phenotype by NET4A could also be observed on the organ level, indicated by longer roots of *act7-4* x NET4A-GFP^{OE} compared to *act7-4* (Fig 2D). Interestingly, while root length for the *act2 act8* mutant was inconspicuous, the observed wavy root phenotype could be largely reversed by NET4A overexpression (Fig 2E).

This suggests that higher NET4 abundance leads to increased recruitment of actin filaments, which compensate for the loss of certain vegetative actin isoforms such as *ACTIN 2, ACTIN7* and *ACTIN 8*.

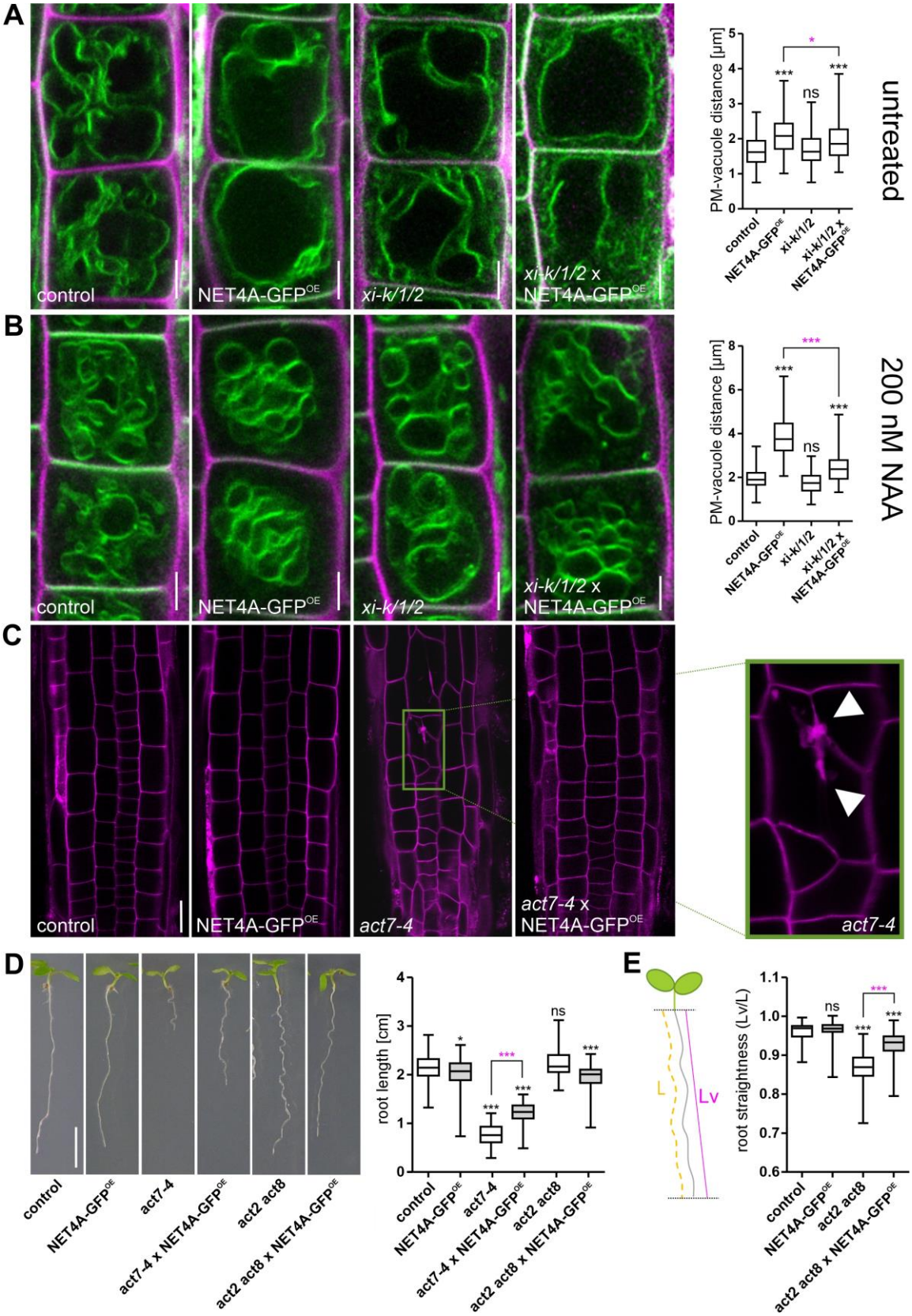

Figure 2 Recovery of actin related phenotypes by NET4 overexpression. A, PM to tonoplast distance in dependence of NET4A overexpression and myosin triple knockout mutant (*xi-k/1/2*). n=124 cells from 31 seedlings for control, n=132 cells from 33 seedlings for NET4A-GFP^{OE}, n=124 cells from 31 seedlings for *xi-k/1/2*, n=136 cells from 34 seedlings for *xi-k/1/2* x NET4A-GFP^{OE}. B, Effect of exogenous auxin (NAA) on PM to tonoplast distance. n=92 cells from 22 seedlings for control, n=92

cells from 22 seedlings for NET4A-GFP^{OE}, n=96 cells from 24 seedlings for *xi-k/1/2*, n=76 cells from 19 seedlings for *xi-k/1/2* x NET4A-GFP^{OE}. The tonoplast is stained with MDY-64, cell walls are stained with propidium iodide (PI). Scale bars = 5 µm (A and B). C, Cellular organization of the epidermis in the Arabidopsis root meristem in dependence of NET4A-GFP^{OE} and the actin mutant *act7-4*. Cell walls are highlighted by PI and arrowheads depict disorganization of cell walls in the mutant. Scale bar = 20 µm. D, Effect of NET4A overexpression on root length of actin mutants. n=153 for control, n=154 for NET4A-GFP^{OE}, n=48 for *act7-4*, n=59 for *act7-4* x NET4A-GFP^{OE}, n=57 for *act2 act8* and n=57 for *act2 act8* x NET4A-GFP^{OE}. Scale bar = 5 mm. E, Quantification of *act2 act8* root straightness in dependence of NET4A overexpression. n=60 for control, n=60 for NET4A-GFP^{OE}, n=57 for *act2 act8* and n=57 for *act2 act8* x NET4A-GFP^{OE}. Box limits in all graphs represent 25th-75th percentile, the horizontal line the median and whiskers minimum to maximum values. Significant differences compared with the wild type (control) are shown (one-way ANOVA and Tukey post hoc test; $^{*}P < 0.05$; $^{***}P < 0.001$). Selected differences between lines are highlighted in magenta (based on one-way ANOVA and Tukey post hoc test).

NET4A localizes to vacuole-vacuole connection sites, regulating homotypic fusion

To investigate NET4 localization at the tonoplast under actin-depleting conditions, we pharmacologically interfered with filament formation by using the marine toxin latrunculin B (LatB). It has been previously shown that LatB treatment leads to vacuole fragmentation, inducing numerous small isolated vacuolar structures (Scheuring et al., 2016). While NET4 localized in a bead-on-a-string pattern at the tonoplast (Fig 3A), LatB treatment led to an accumulation of NET4 signals at specific foci, at which vacuolar substructures seem to be physically connected (Fig 3B). This might indicate a NET4 recruitment to distinct tonoplast areas, presumably where (homotypic) vacuole fusion occurs. Consequently, overexpression of NET4 should allow for more efficient fusion. To test for this, we induced vacuole fragmentation by LatB treatment and investigated changes of vacuolar morphology. To highlight the vacuolar lumen, we used the dye BCECF (Scheuring et al., 2015) and monitored morphology in the *net4a net4b* double mutant and in the NET4A overexpression line compared to Col-0 wt as control. As expected, LatB induced fragmentation of vacuoles in the control. However, NET4A-GFP^{OE} was largely resistant against LatB, displaying vacuoles of almost unchanged size and shape (Fig 3C and 3D). The approximated vacuole size in control and *net4a net4b* significantly decreased and the number of vacuolar structures increased in parallel; the latter, however, to a lower extent in the double mutant (which already showed more structures under untreated conditions). NET4A-GFP^{OE} vacuoles on the other hand remained larger and the already fewer numbers under normal conditions hardly increased (Fig. 3E and 3F). This LatB resistance could be confirmed on the level of root growth, where LatB-dependent growth inhibition of the overexpressor but also that of the double mutant was significantly reduced (Fig. 3G). When monitoring lifeact-RFP during LatB treatment, we observed a seemingly slower actin filament depolymerization in the NET4A-GFP^{OE} background (Supplementary Fig S4).

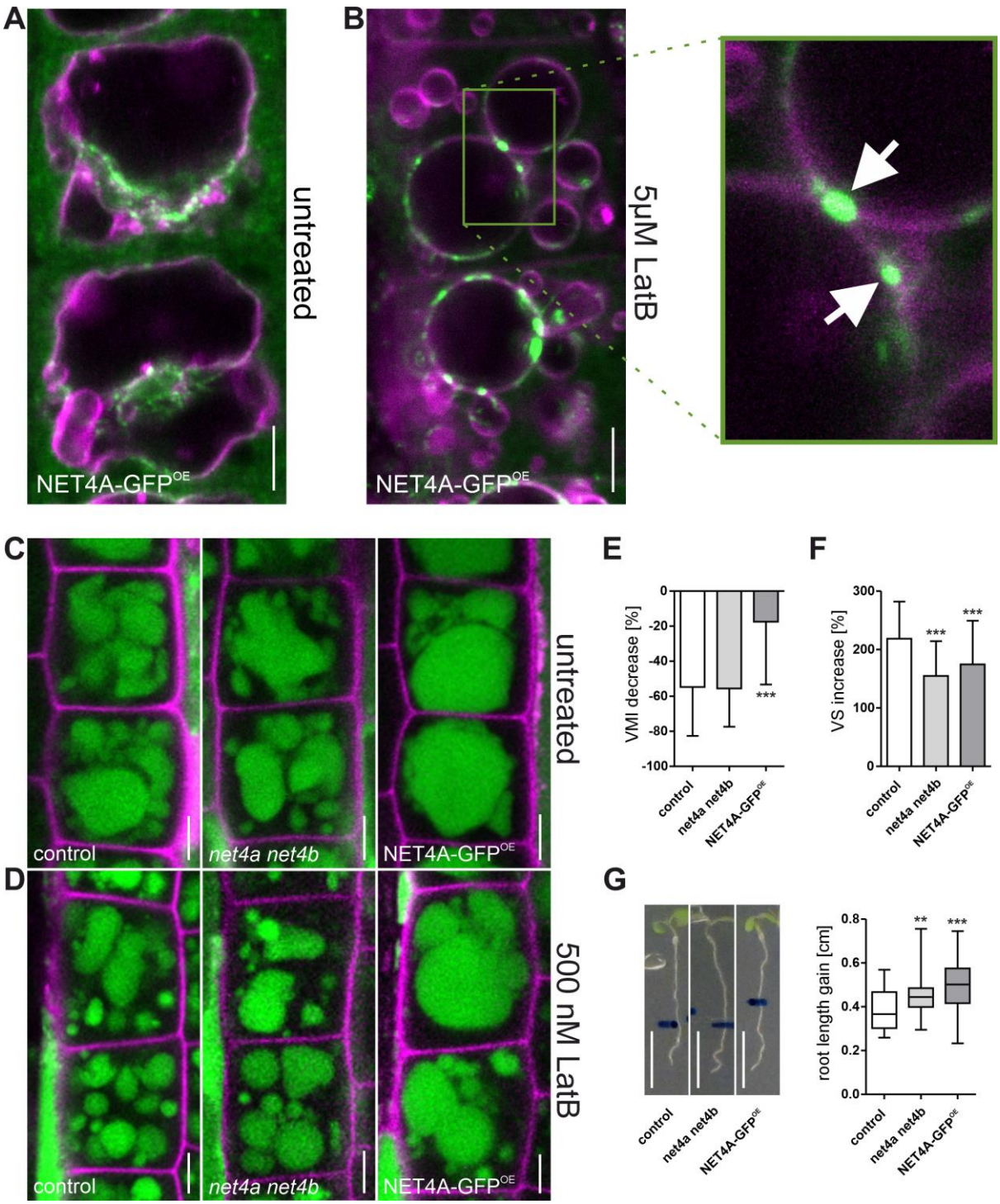

Figure 3 NET4 localizes to vacuole connections and impacts actin stability. A, Tonoplast staining by FM4-64 in the NET4A-GFP^{OE} background. B, 5 µM LatB treatment (5h) to depolymerize actin. C, Vacuoles stained by BCECF in cells (stained by PI) of Col-0 (control), the *net4a net4b* double mutant and the NET4A-GFP^{OE} line. D, LatB impact (5h) on vacuolar morphology. E, Quantification of vacuolar morphology index (VMI) changes. F, Quantification of the relative number of vacuolar structures (VS). n=97 cells from 20 seedlings for control, n=86 cells from 20 seedlings for *net4a net4b* and n=112 cells from 18 seedlings for NET4A-GFP^{OE}. G, Root growth (48h) upon seedling transfer of 4-days-old plants on 50 nM LatB containing half-strength MS medium plates. n=54 for control, n=52 for *net4a net4b* and n=47 for NET4A-GFP^{OE}. Scale bars = 5 µm (A-D) and 5 mm (G). Bar chart columns display mean values and error bars the standard deviation. Box limits in all graphs represent 25th-75th percentile, the horizontal line the median and whiskers minimum to maximum values.

Significant differences compared with the wild type (control) are shown (one-way ANOVA and Dunnett´s post hoc test; *$P < 0.05$; **$P < 0.01$; ***$P < 0.001$).

More compact vacuoles, recovery of mutants with impaired cytoskeleton organization and partial resistance to vacuole changes by actin depolymerization led us to hypothesize that NET4 participates in membrane fusion events at the tonoplast. To test for this, we used *amiR-vps16,* a conditional, on artificial microRNA (amiR) based, mutant of the VPS16 subunit from the HOPS tethering complex and crossed it with NET4A-GFP^{OE}. Vacuolar morphology was assessed upon knock down by Dexamethasone (DEX)-induced expression of the specific amiR. This resulted in fragmented vacuoles for *amiR-vps16* as reported for *amiR-vps39* (Takemoto et al., 2018). In contrast, vacuole fragmentation was significantly reduced in the crossed line (compare Fig 4A and 4B), confirming a role for NET4 in fusion processes at the vacuole. Trafficking towards and fusion with the vacuole requires the recruitment of fusiogenic proteins which is initiated by activated GTPases RAB5 and RAB7 (RABF and RABG in plants) (Aniento et al., 2022). Since RABG3 proteins directly interact with the VPS39 subunit of the HOPS complex (Takemoto et al., 2018), we took advantage of the already existing *rabg3a,b,c,d,e,f* sextuple mutant (Ebine et al., 2014) and investigated vacuolar morphology (Fig 4C and 4D). Additionally, we knocked out *NET4A* in the mutant background creating two septuple mutants. The sextuple as well as the two septuple mutants showed large vacuolar bodies in the cell centre with numerous smaller, possibly disconnected vesicles in the periphery. Sometimes, and more often for the septuple mutants, the large vacuole body appeared to be replaced by two or more smaller vacuole parts (Fig 4C, Supplementary Fig S5A). Notably, root length of sextuple and septuple mutants was severely reduced (Supplementary Fig S5B). To address the cytological basis for these structural changes, we used 3D reconstructions of epidermal cell vacuoles. While control cells showed largely interconnected vacuolar cisternae as reported previously (Scheuring et al., 2016), the sextuple and even more pronounced the analyzed septuple mutant displayed non-fused, disconnected vacuolar substructures/vesicles which in the latter case occupied less cellular space (Fig 4E).

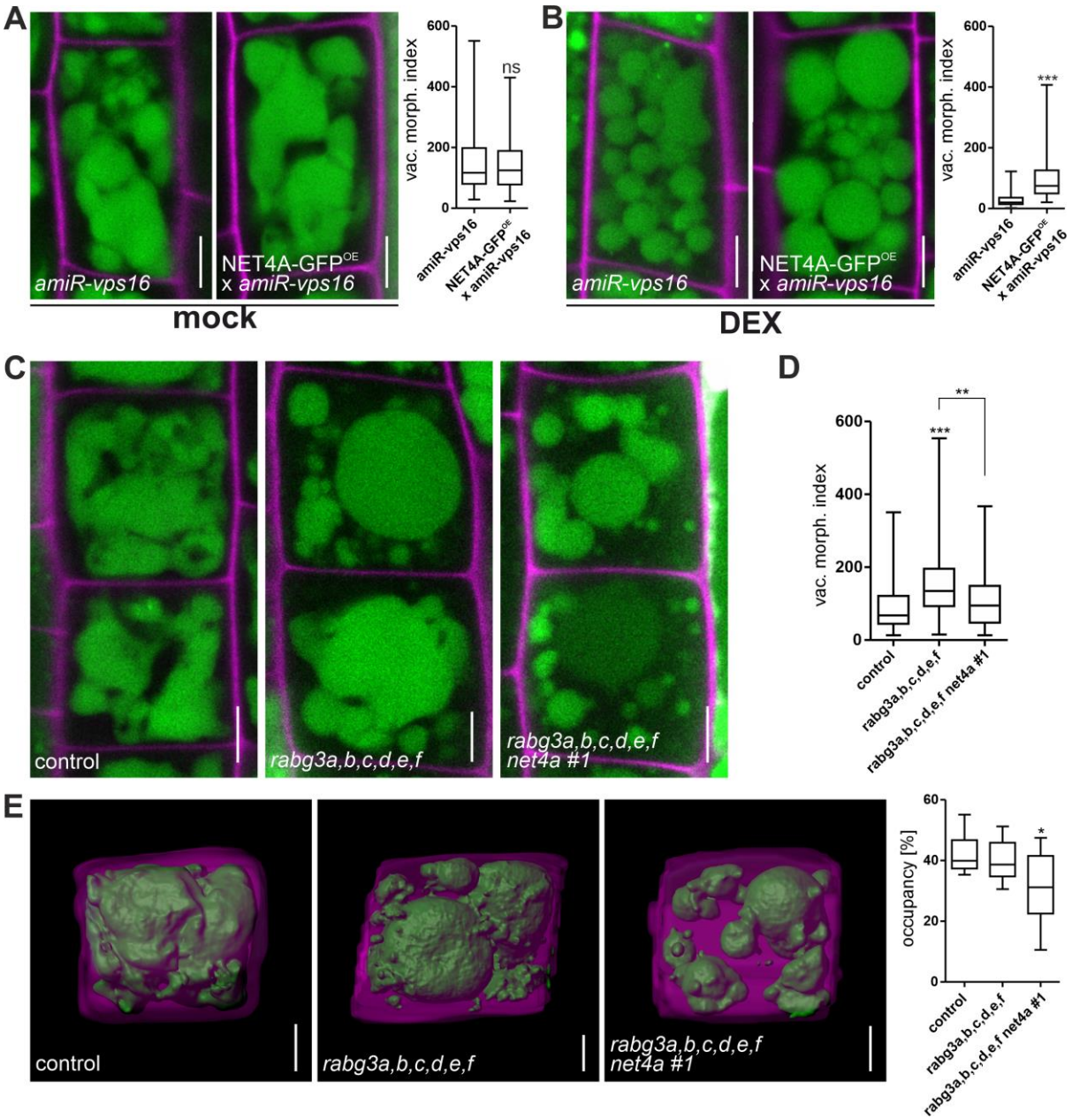

Figure 4 NET4 participates in vacuole fusion events. Conditional knockdown of HOPS and CORVET subunits induces vacuole (stained by BCECF) fragmentation. A, Vacuolar morphology upon knock down of *VPS16* by DEX induction of amiRNA in comparison to the same line crossed with NET4A-GFP^{OE}. B, Quantification of vacuolar morphology index (VMI) for *amiR-vps16* and NET4A-GFP^{OE} x *amiR-vps16* under mock (n=109 and 107) or DEX treatment (n=100 and 97). C, Vacuolar morphology of the *rabg3a,b,c,d,e,f* sextuple and the *rabg3a,b,c,d,e,f net4a #1* septuple mutant compared to Col-0 wild type (control). D, Quantification of (C) using the VMI (n=96 for control, 100 for *rabg3a,b,c,d,e,f* and *92* for *rabg3a,b,c,d,e,f net4a #1)*. E, 3D reconstruction of cells and vacuoles as well as quantification of the vacuolar occupancy of cells for control (n=8), *rabg3a,b,c,d,e,f* (n=9) and *rabg3a,b,c,d,e,f net4a #1* (n=9). Box limits represent 25th-75th percentile, the horizontal line the median and whiskers minimum to maximum values. Significant differences are shown and were analyzed by Student's t-test (A, B) or one-way ANOVA and Tukey post hoc test (D, E); *$P < 0.05$; **$P < 0.01$; ***$P < 0.001$. Scale bars = 5 µm.

NET4 interacts with RAB-GTPases and unknown proteins

To unravel how NET4 connects to the HOPS complex and RABG3 GTPases, we searched for NET4A interaction partners. To this end, we carried out co-immunoprecipitation

followed by MS-MS analysis. Using NET4A-GFP (endogenous promoter) and NET4A-GFP^{OE} lines (35S promoter), several proteins co-precipitated with the NET4A-GFP fusion protein and were significantly enriched compared to the wt control (Fig 5A and 5B). Among them were two proteins with unknown function (At2g15042 and At4g01245), RABC1 and two RABG3-GTPases. Interestingly, while RABG3-GTPases are localized at multivesicular bodies and the vacuole, RABC1 is considered a *bona fide* marker for the *trans*-Golgi network (Geldner et al., 2009), suggesting a NET4 function in addition to its function at the vacuole. To confirm the interactions, ratiometric Bimolecular Fluorescence Complementation (rBiFC) measurements in transiently transformed *N. benthamiana* were carried out. Except for At2g15042, all tested interactions could be confirmed albeit signal strength was differing (Fig 5C). In addition, testing the same combinations, this finding was confirmed using the mating-based Split-Ubiquitin System (mbSUS) (Grefen et al., 2009) in yeast (Supplementary Fig S6).

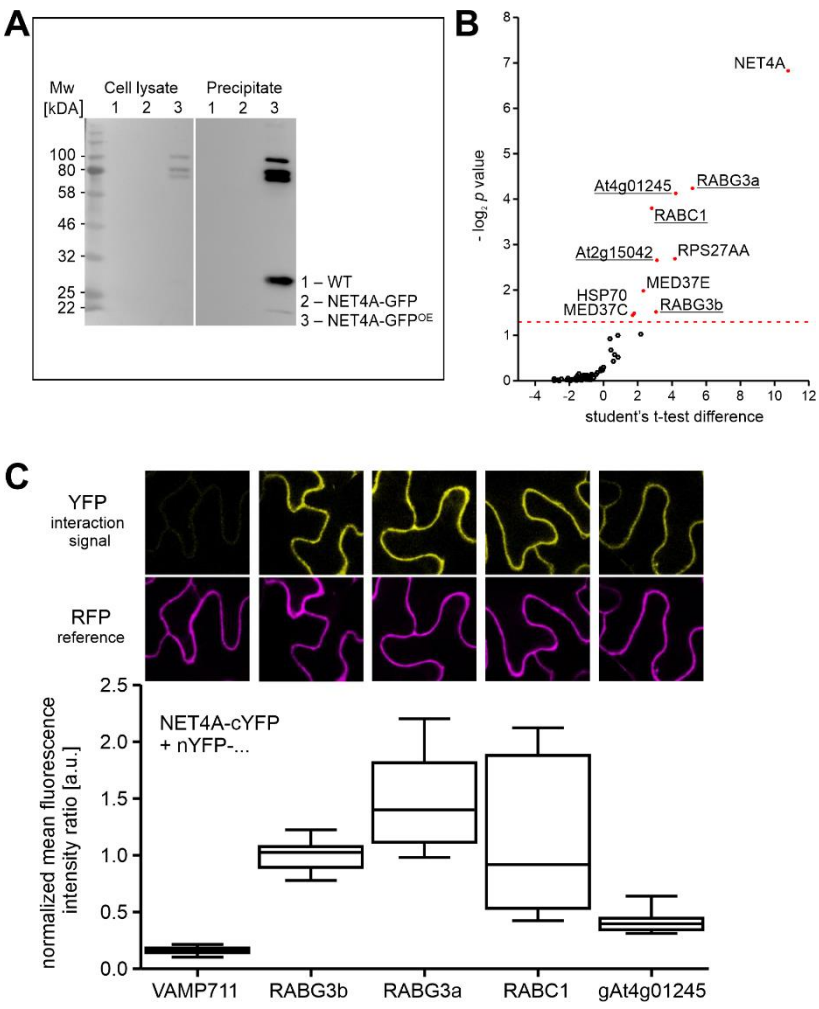

Figure 5 Identification and confirmation of NET4A interaction partners. A, Detection of NET4A-GFP fusion protein for the indicated lines using a GFP specific antibody after co-immunoprecipitation of NET4A-GFP interaction partners with GFP-trap magnetic agarose beads. B, LC-MS/MS-based identification of proteins that were co-immunoprecipitated with NET4A-GFP. The dashed line marks the threshold for significant increase in protein abundance compared to the wild type (control). Proteins used for confirmation are underlined. C, Representative images and quantification of ratiometric bimolecular fluorescence complementation (rBiFC) measurements in *N. benthamiana* leaf epidermis cells. For quantification, YFP signals were normalized to the respective RFP signals to allow comparison of interaction strength. VAMP711, a SNARE localized to the tonoplast was used as negative control.

In order to interact, NET4 and partners must at least partially colocalize. All NET proteins are cytosolic proteins, which are recruited to their target membranes post-translationally. To investigate the possibility of NET4 membrane binding, we conducted

protein-lipid overlay assays. For detection, a NET4 antibody was generated against the full length NET4A protein. To test for specificity, we could show that the antigen is recognized as well as the native protein and GFP-fusion proteins in plant cell extracts when using the anti NET4 antibody (Supplementary Fig S7A). Immunoblotting with an anti GFP antibody showed signals corresponding to the right size only in extracts from GFP-fusion lines (Supplementary Fig S7B). When incubated with a lipid array, NET4 interacted with all negatively charged phospholipids, namely phosphoinositides (PIPs) and phosphoatidic acid (PA) (Supplementary Fig S7C). This was confirmed by using an anti HIS antibody for detection of HIS-tagged NET4A (Supplementary Fig S7D). Since individual PIPs are differentially distributed in the endomembrane system and thereby contribute to organelle identity (Noack and Jaillais, 2017), binding of NET4A to all PIPs was casting doubts on its exclusive function in connection with the vacuole.

NET3 and NET4 redundantly interact with tonoplast-residing RABG3s and ER membrane integral VAP27-1

Recently, it has been shown that NET4 interacts with active RABG3 members, indicating that vacuole membrane recruitment of NET4 occurs via this binding (Hawkins et al., 2023) . The authors could show that RABG3-binding requires a so-called IRQ-domain, which is present not only in NET4A and NET4B but also in NET3A and NET3C. To investigate membrane recruitment of NET4, we generated truncated GFP-tagged versions of NET4A covering its entire length (Fig 6A). While the Networked-specific actin binding (NAB) domain highlighted filaments as expected, aa 106-503, the middle part of NET4A, showed cytosolic localization and signals at the nuclear envelope (Fig 6B), which colocalized with the ER marker RFP-HDEL during coexpression in *N. benthamiana* leaf epidermal cells (Fig 6C). Intriguingly, the IRQ domain expressed alone (aa 504-542) also highlighted the nuclear envelope (Fig 6B and 6C) and addition of the C-terminus (aa 504-558) was sufficient to result in a clear tonoplast signal (Fig 6B). This is in agreement with published data showing that the IRQ domain plus the C-terminus together are required for RABG3 binding (Hawkins et al., 2023). Performing mbSUS growth assays in yeast, we could also confirm NET4-binding to different RABG3s (Supplementary Fig S6, Fig 6D). Intriguingly, we also found NET3A and NET3C to interact with RABG3A and RABG3B (Fig 6E, Supplementary Fig S8). This finding, together with localization of NET4 truncations at the nuclear envelope, led us to hypothesize that both NET families might be able to carry out exchangeable functions. Therefore, we tested whether NET4 is found at the ER in addition to its association to the tonoplast (Kaiser et al., 2019). To this end, we transiently coexpressed full length NET4A-mTurquoise and NET4B-GFP individually with the ER marker RFP-HDEL. In both cases, a

partial colocalization specifically at the nuclear envelope could be observed (Supplementary Fig S9). In addition, we could confirm NET4 at the nuclear envelope by crossing NET4A-GFP expressing Arabidopsis lines with ER marker lines expressing RFP-HDEL or SRß-mTurquoise, a subunit of the signal recognition particle at the ER membrane (Fig 6F).

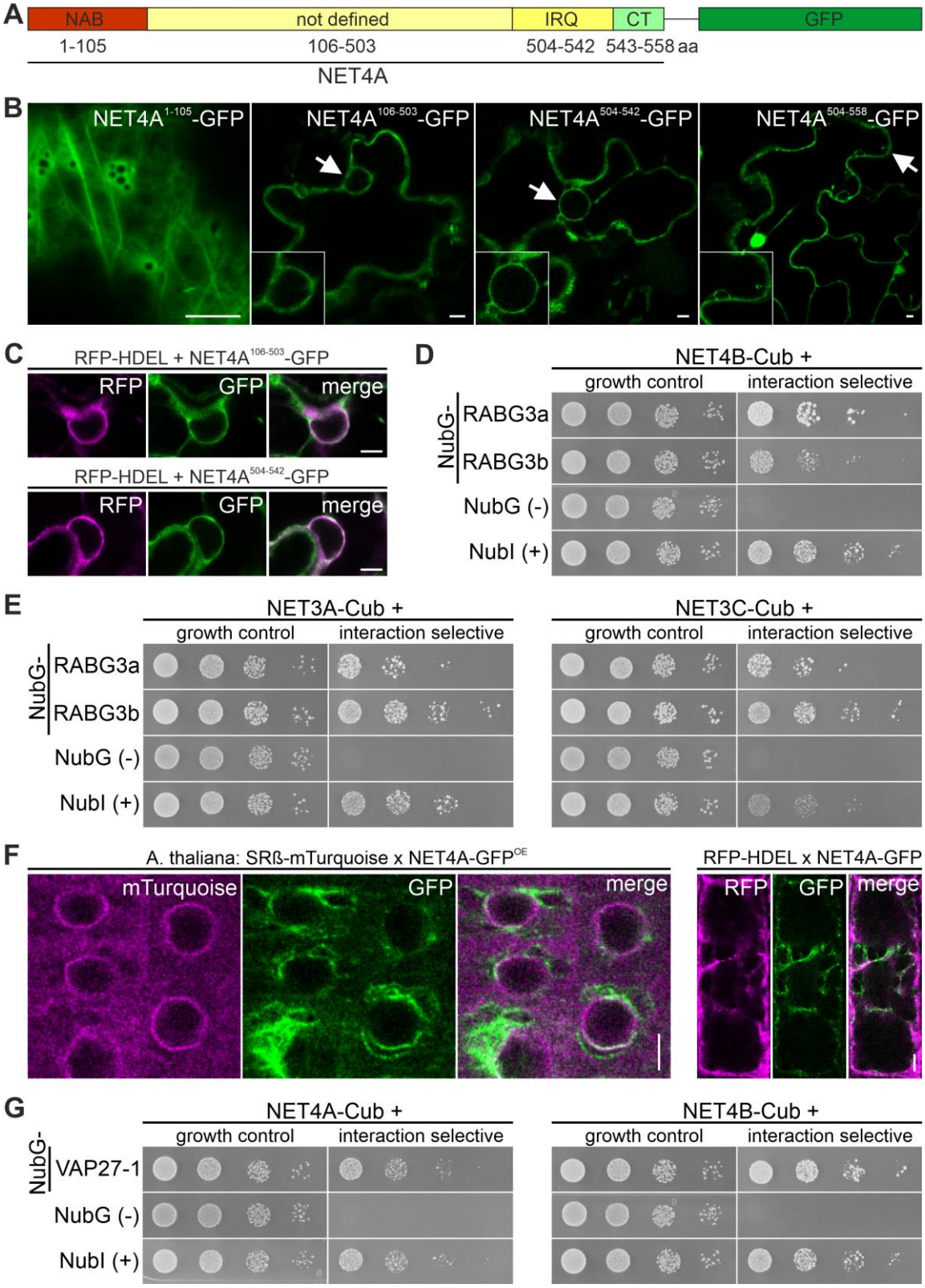

Figure 6 NET3 and NET4 display interchangeable functions. A, Schematic representation of the NET4 domain structure. B, Localization of shortened NET4A upon transient gene expression in *N. benthamiana.* C, Colocalization of either NET4A$^{105-503}$-GFP or NET4A$^{504-542}$-GFP with the ER marker RFP-HDEL upon transient coexpression in *N. benthamiana*. D and E, mating-based Split-Ubiquitin System (mbSUS) growth assays in yeast using NET4B-, NET3A- and NET3C-Cub to test for interaction with NubG-RABG3A and -RABG3B. F, NET4A-GFP^{OE} (35S-promoter) and NET4A-GFP (endogenous promoter) were crossed with the ER marker SRß-mTurquoise and RFP-HDEL, respectively, and colocalization was determined. G, mbSUS growth assays testing NET4A- and NET4B-Cub for NubG-VAP27-1 interaction. For mbSUS growth assays (D, E and G) THY.AP4 (MATa) yeast strains transformed with Cub-fusions were mated with THY.AP5 (MATα) strains transformed with NubG-fusions. Growth was assayed in dilution series of OD_{600} from 1 to 0.001 at 28°C on growth control media for 36 h to confirm presence of vector fusion constructs and interaction selective media for 72 h to test for specific interaction dependent activation of the reporter genes. NubG was used as negative, NubI as positive control. Note: Nub controls for NET4B in D and G are identical since they are from the same plate. Scale bars: 5 µm.

Since it has been shown that NET3C recruitment to the ER is mediated by its interaction with the ER-resident VAP27-1 (Wang et al., 2014), we tested whether NET4 can also interact with VAP27-1. Yeast mbSUS growth assays confirmed the interaction of both, NET4A and NET4B, with VAP27-1, supporting their presence at the nuclear envelope (Fig 6G).

Higher order NET3-NET4 mutants display impaired vacuolar morphology and reduced growth

Following the hypothesis that NET3 and NET4 families might carry out overlapping functions, higher order NET3/NET4 mutants were generated using either T-DNA insertion mutants or newly generated mutants. To this end, we established a modified CRISPR/Cas9 protocol harbouring fluorescent seed coat markers for efficient detection of transformants. Gene deletions of *NET3A* and *NET3C* in wild type and *net4a net4b* (T-DNA) background as well as full-CRISPR *net3c net4a net4b* deletion lines were established.

Notably, gene expression of *NET4A* and *NET4B* seemed to be remarkably different on the organismal level. While *NET4A* expression started in the transition zone of the root and hardly showed expression in aerial tissue, *NET4B* was expressed strongly in the root meristem and in guard cells of cotyledons (Supplementary Fig S10 and S11). Since *NET4* and *NET4B* expression in most parts of young seedlings seemed to be mutually exclusive, we monitored general growth defects in the established mutants. Phenotypic analysis revealed that the full-CRISPR *net3c net4a net4b* mutant but neither *net3c* alone nor *net3a* (CRISPR) *net4a net4b* (T-DNA) mutants (Supplementary Fig 12), displayed decreased VMI and vacuolar occupancy (Fig 7A and Fig 7B) together with inhibited root growth (Fig 7C).

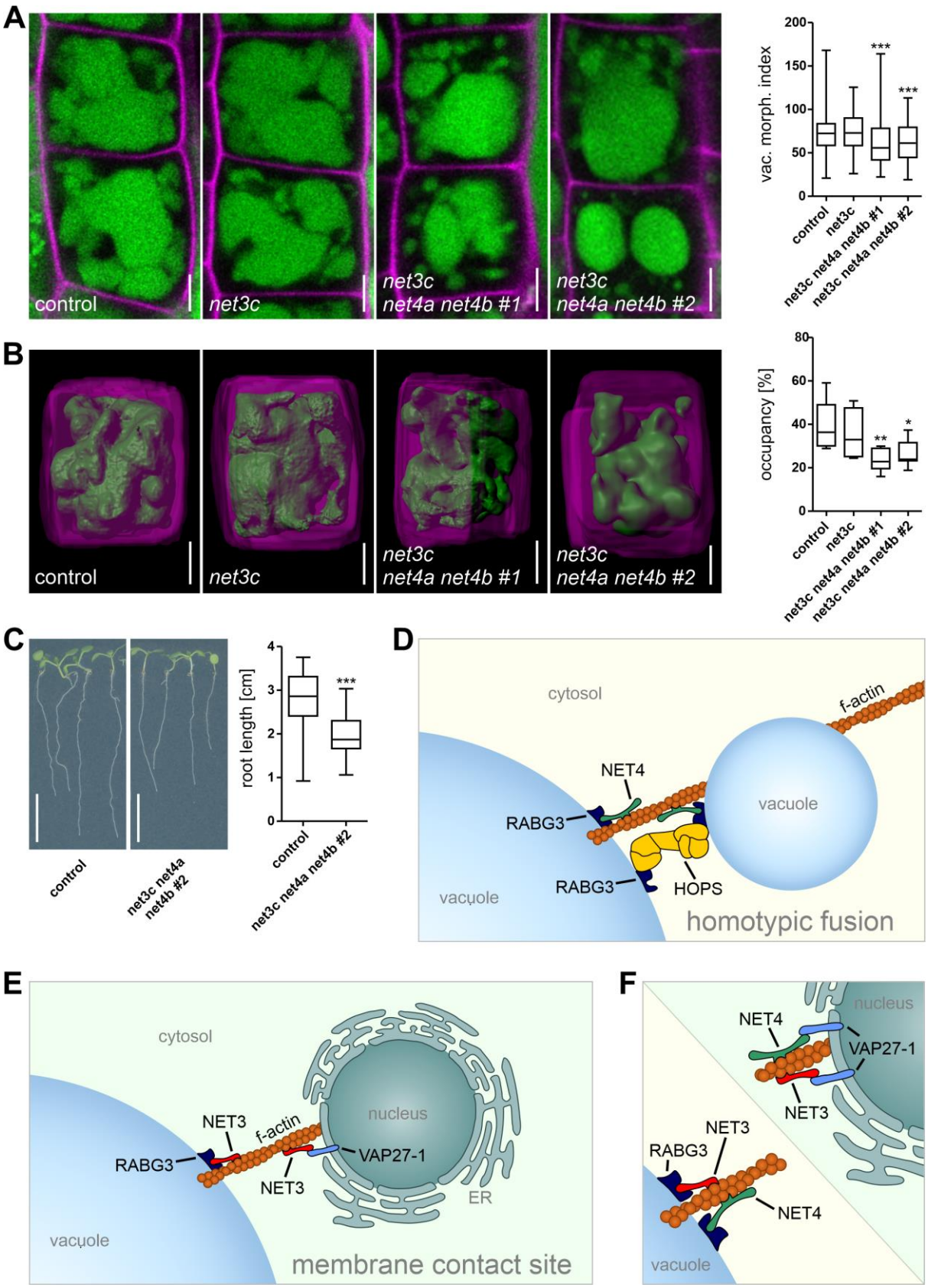

Figure 7 Phenotypic analysis of NET3-NET4 multiple mutants and working model of NET4 function. A, Investigation of vacuolar morphology for lines with CRISPR/Cas9 derived deletion of *NET3C* in Col-0 wild type (*net3c,* n=84), *net4a net4b* t-DNA mutant (*net3c net4a net4b #1*, n=88) and also CRISPR/Cas9 derived deletions of *NET4A* and *NET4B* (*net3c net4a net4b #2*, n=124) compared to Col-0 control (n=212). B, 3D vacuole and cell reconstructions and quantification of vacuolar

occupancy for Col-0 control (n=6), *net3c* (n=6), *net3c net4a net4b #1* (n=8) and *net3c net4a net4b #2* (n=7). Box limits represent 25th-75th percentile, the horizontal line the median and whiskers minimum to maximum values. Significant differences are shown and were analyzed by one-way ANOVA and Dunnett's post hoc test; $*P < 0.05$; $**P < 0.01$; $***P < 0.001$. Scale bars = 5 µm for (A) and (B). C, Root growth of 6 days old Arabidopsis seedlings for Col-0 control (n=55) and *net3c net4a net4b #2* (n=49). Scale bar = 1 cm. D, Working model indicating homotypic vacuole fusion: NET4 binds actin filaments and is recruited via its IRQ domain to vacuole-bound RABG3. Binding of RABG3 to the HOPS tethering complex will allow membranes to come into close proximity and SNARE-interaction will mediate membrane fusion. E, The ability of ER-localized NET3A or NET3C to bind RABG3 at the vacuole connects these organelles, but since neither HOPS tether complex nor the correct set of SNAREs are present at the ER, no fusion will occur. This could potentially represent an unknown and plant specific membrane contact site between the ER and the lytic vacuole. F, Since NET4 is able to bind the membrane contact site protein VAP27-1 at the ER, functional redundancy of NET3 and NET4 occurs at both locations, tonoplast and ER.

Discussion

NET4A reorganizes actin filaments towards the nuclear envelope compensating defects in actin mutants

Our previous findings indicate that the vacuole-cytoskeleton interface is crucial to regulate vacuolar morphology and relative vacuole size (Scheuring et al., 2016). The present data indicate that remodeling of actin filaments contributes to shape the vacuole. More compact vacuoles of NET4 are accompanied by actin filaments focused towards the nucleus (Fig 1). Thus, in addition to the original description that NET4 accumulates at sites of vacuolar constrictions (Kaiser et al., 2019), NET4 seems to be especially abundant next to the nucleus. Enhanced recruitment of actin filaments towards the cells' centre can compensate for the loss of vegetative actin isoforms such as *ACTIN 7* (Fig 2). *ACT7* has been shown to be specifically involved in root growth and root architecture as well as being highly responsive towards treatment with the plant hormone auxin (McDowell et al., 1996; Kandasamy et al., 2009). Actin filaments recruited towards the nuclear envelope by NET4A-GFP^{OE} are in close proximity of the nucleus, which could indicate a function in nucleus positioning. In animal cells, maintaining nuclear shape and position requires lamins, a type of intermediate filaments which do not exist in plants (Gundersen and Worman, 2013). In plants, nucleus positioning in root hairs has been reported to depend on filamentous actin organization (Ketelaar et al., 2002; Chytilova et al., 2000). Thus, we tested nucleus positioning in NET4A-GFP^{OE} and *net4a net4b* but could not detect any changes in epidermal root cells of the meristem (data not shown). However, limited vacuole fragmentation (Fig 3) and slower actin depolymerisation (Supplementary Fig S4) upon LatB treatment strongly suggests a stabilizing function of NET4A at the tonoplast.

NET localizes to fusion sites at the vacuole

It has been shown that organelle-bound actin is required for vacuole fusion events in yeast (Eitzen et al., 2002). Prior to fusion, vacuoles come close, thereby forming the so-

called boundary membrane, which resembles a flattened disc. The edge of this boundary is termed the vertex ring, where lipids and fusogenic proteins (responsible for fusion) accumulate (Starr and Fratti, 2019). Intriguingly, upon vacuole disassembly by LatB, NET4 signals at contact sites of still docked vacuoles strongly resemble these vertex rings (Fig 3). In yeast, vertex rings accumulate lipids such as phosphoinositides and ergosterol but also actin becomes enriched (Eitzen et al., 2002). After phosphoinositide enrichment (phosphatidylinositol 3-phosphate, PI3P), a Rab7-GTPase is recruited to the vacuolar membrane (Wickner, 2010). The HOPS-specific subunits Vps39p and Vps41p subsequently bind to Rab7 and allow for assembly of the SNARE proteins and eventually membrane fusion (Balderhaar and Ungermann, 2013). The interaction with RABG3a and RABG3b directly links NET4 to specific fusion sites at the vacuole (Fig 5, Supplementary Fig S6). Since NET4A overexpression partially rescued HOPS knockdown and *NET4A* deletion enhanced the fusion-defective RABG3 sextuple mutant, it is possible that NET4 defines actin anchor points at vertex rings. Interestingly, upon HOPS knockdown, connections between vacuolar substructures were lost and several, fragmented and entirely spherical vacuoles occurred.

Identification of interaction partners

The identification of four interaction partners, which are localized to different organelles, suggests additional functions for NET4 apart from connecting actin to the tonoplast. We hypothesize that depending on the interaction partner, adaptor complexes of different composition can be formed to connect different organelles via actin filaments (Fig 7D-F). Prior to the formation of PM-ER contact sites, several proteins (including NET3C, VAP27, KLCR1 and IQD2) have been shown to interact, forming adaptor complexes to bridge the cytoskeleton with the respective organelles (Zang et al., 2021). NET3 proteins have been demonstrated to reside close to the nucleus, at the ER and the nuclear envelope, where they form membrane contact sites, connecting the PM with the ER via the cytoskeleton (Wang et al., 2014; Zang et al., 2021). Notably, a so-called IRQ domain has been identified in NET3A and NET3C which is also present in the tonoplast-residing NET4A and NET4B (Hawkins et al., 2023). While it has been shown already that NET4A and NET4B interact with active RABG3s via this domain (Hawkins et al., 2023), we could extend this finding demonstrating that the ER-resident NET3A and NET3C interact with tonoplast residing RABG3 GTPases as well. Together with the partial ER-localization of NET4 and its ability to interact with the ER-PM contact site protein VAP27 (Wang et al., 2014), this establishes a direct connection between the ER and the vacuole. This could represent an efficient way to provide ER-derived lipids to the expanding vacuole or to deliver distinct sets of proteins to developing (pro-) vacuoles (Viotti et al., 2013; Minina et al., 2021). NET3- and

NET4-mediated bridging of the ER and the vacuole to establish a membrane contact site would be novel in plants. A lysosome-ER contact site has just been demonstrated for animal cells (Tan and Finkel, 2022). Interestingly, although RABC1 has been used as marker for the *trans*-Golgi network (Geldner et al., 2009), it has been localized to the ER as well lately (Ge et al., 2022).

NET3 and NET4 function redundantly and seem to be involved in the generation of an ER-vacuole membrane contact site.

The (at least partial) functional redundancy between NET3 and NET4 might also explain the lack of an obvious and global *net4a net4b* phenotype (Kaiser et al., 2019; Hawkins et al., 2023). While none of the other NET superfamily members were transcriptionally upregulated in the *net4a net4b* background (Kaiser et al., 2021), compensation could be achieved by NET3s on the protein level. Only the generation of multifold *net3 net4* mutants resulted in a clear phenotype on different levels (Fig 7). The presence of numerous small vacuolar structures and the smaller relative size (occupancy) of the *net4a net4b net3c* triple mutant lines suggests disturbance of homotypic fusion processes. In addition, restricting vacuolar occupancy of the cell seems likely to be the cause for impaired root growth, since it interferes with the space-filling-function of the vacuole as reported previously (Kaiser and Scheuring, 2020).

Taken together, NET4 seems to participate in homotypic vacuole fusion events by interacting with the HOPS complex via RABG3 binding (Fig 7D). In addition, NET3 and NET4 proteins redundantly form complexes with RABG3-GTPases, VAP27-1 and actin filaments, potentially to establish a, yet unknown and plant-specific, membrane contact site between the ER and the vacuole (Fig 7E and F). This direct connection would allow direct lipid and protein transfer, which is especially important in young and expanding cells. Here, the availability of lipids would facilitate a rapid expansion of vacuoles, which are the basis for high cell elongation rates and fast plant growth.

Material and Methods

Plant Material and Growth Conditions

Arabidopsis thaliana ecotype Columbia-0 (Col-0) was used as wild type control. The following lines were described previously: lifeact-RFP (Rosero et al., 2016), 35S::NET4A-GFP (NET4A-GFP^{OE}) (Kaiser et al., 2019), NET4A::NET4A-GFP (NET4A-GFP) (Deeks et al., 2012), RFP-HDEL, *xi-k/1/2* (Peremyslov et al., 2010), *act7-4* (Gilliland et al., 2003), *act2 act8* (Kandasamy et al., 2009), *net4a net4b* (Kaiser et al., 2019) and *rabg3a,b,c,d,e,f* (Ebine et al., 2014). Seeds were surface sterilized with ethanol and plates were stratified at 4 °C for 1–2 days in the dark and grown vertically at 22 °C under a 16 h light/8 h dark-cycle. For seedling growth, half-strength Murashige and Skoog (MS) medium (Duchefa,

Netherlands), including 1% (w/v) sucrose (Roth, Germany), 2.56 mM MES (Duchefa) and 1% (w/v) Phytoagar (Duchefa) was used at pH 5.7.

Chemicals and Treatments

The dyes MDY-64, propidium iodide (PI), FM4-64 and BCECF-AM were acquired from Life Technologies (CA, USA). The synthetic auxin α-Naphthaleneacetic acid (NAA) and dexamethasone (DEX) were obtained from Duchefa and latrunculin B (LatB) from Sigma-Aldrich (MO, USA). Except PI, all chemicals were obtained in powder form and dissolved in dimethyl sulfoxide (DMSO).

RNA Extraction and Quantitative Real Time PCR

RNA extraction and transcription into cDNA was carried out as described previously (Jeblick et al., 2023). For qRT-PCR, the PerfeCTa SYBR Green SuperMix for iQ (Quanta BioSciences, USA) was used and reactions were carried out in a CFX Connect Real-Time PCR Detection System (Bio-Rad, USA). Reaction procedures were set to an initial heating step of 95 °C for 3 min as well as 40 cycles of denaturing at 95 °C for 10 s followed by combined annealing-extension at 60 °C for 40 s. Primers used for target and housekeeping genes (*PP2A*) are shown in Supplemental Table S1. To calculate relative expression ratios, the efficiency corrected calculation model was used (Pfaffl, 2001).

Cloning

All expression constructs were generated using the GreenGate system (Lampropoulos et al., 2013) and are listed in Supplemental Table S2. Primers used to amplify sequences for the creation of new GreenGate entry vectors are given in Supplemental Table S3. GFP, mTurquoise and mCherry modules (pGGD011, pGGD-GSL-mTurquoise, pGGD010 and pGGF Alli-mCherry) were published before (Lupanga et al., 2020; Stührwohldt et al., 2020; Waadt et al., 2017; Stephani et al., 2020). Internal *Bsa*I sites were mutated. To this end, additional internal primers were used to introduce suitable silent point mutations during the amplification of separate sequence parts, and the resulting PCR products were fused. In case *Bsa*I sites were present in promoter sequences, no entry vector was generated. Instead, the sequence was amplified using suitable primers to produce matching overhangs by using alternative restriction enzymes. Subsequently, the final construct was generated preassembling all modules without the promoter module. Later, the promoter sequence with matching overhangs was added by ligation in a separate reaction. A list of all entry modules generated is provided as Supplemental Table S4. The DEX-inducible amiRNA based knockdown constructs for *VPS16* (*amiR-vps16*) was cloned as described for other *VPS* (Takemoto et al., 2018). Primers used to amplify intermediate and final amiR sequences against *VPS16* are listed in Supplementary Table S5. Deletion mutants were obtained using the egg cell-specific promoter-controlled CRISPR/Cas9 cloning system based on the vector pHEE401E (Wang et al., 2015). To improve the screening for transformed plants, the hygromycin resistance cassette of the original vector was replaced by a mCherry seed coat marker cassette from the GreenGate vector pGGF Alli-mCherry (Stephani et al., 2020), resulting in the generation of pHEE-mCherry. To this end, available *EcoRI* and *SacII* restriction sites of pHEE401E were used to cut out the hygromycin resistance cassette. Vector backbone sequences that were thereby deleted in addition to the cassette were amplified by PCR and cloned back together with the PCR-amplified seed coat marker cassette. Used Primers are given in Supplemental Table S6. The web tools CHOPCHOP

(https://chopchop.cbu.uib.no/; (Labun et al., 2016)) and CCTop (https://cctop.cos.uni-heidelberg.de/; (Stemmer et al., 2015)) were used to select suitable guide RNAs (gRNAs). All constructs were generated by inserting a PCR fragment with two gRNAs for the same gene in the used vector as described in Xing et al. (Xing et al., 2014), aiming to delete the region between the two target sites (Supplementary Fig S13). Amplification of the respective insertion fragments was performed using the primers listed in Supplemental Table S7 and vector pHEE2E-TRI as a template. All generated CRISPR/Cas9 constructs are listed in Supplemental Table S8 and details about the used base vector and gRNAs are given. The obtained mutant lines are shown in Supplemental Table S9.
DNA constructs for rBiFC and mbSUS assays were generated via the 2in1 cloning system (Mehlhorn et al., 2018) or Gateway™ technology (Invitrogen, Thermo Fisher Scientific, Carlsbad, CA, USA). Coding sequences were PCR amplified from Col-0 seedling's cDNA or suitable vectors harbouring the sequence. In case of At4g01245, the non-spliced gene was amplified from genomic DNA of Col-0 leaves. All primers are given in Supplemental Table S10. PCR products were recombined into pDONR221-P1P4 or pDONR221-P3P2 for rBiFC and pDONR207 for mbSUS via BP reaction according to the manufacturer's instructions (Invitrogen). Eventually, LR recombination was performed to clone sequences from the generated entry vectors into the appropriate destination vectors pBiFCt-2in1-NC for rBiFC and pNX35-DEST-1 or pMetOYC-Dest for mbSUS. The resulting final constructs are listed in Supplementary Table S11. For recombinant protein expression, the coding sequence of NET4A was amplified from Col-0 cDNA and cloned into pET28a(+) (Sigma-Aldrich) using the restriction sites for *Btg*ZI and *Xho*I. Used primers are given in Supplemental Table S12. All generated constructs were confirmed by sequencing.

Crossing of Arabidopsis and generation of new lines

For generation of stable Arabidopsis plants, *A. tumefaciens* was transformed as described previously (Jeblick et al., 2023), and floral inoculation performed as described by Nurasaka et al. (Narusaka et al., 2010). The lines lifeact-RFP x NET4A-GFP^{OE}, *xi-k/1/2* x NET4A-GFP^{OE}, *act7-4* x NET4A-GFP^{OE}, *act2 act8* x NET4A-GFP^{OE}, NET4A-GFP^{OE} x *amiR-vps16*, SRß-mTurquoise x NET4A-GFP^{OE}, RFP-HDEL x NET4A-GFP were generated by crossing the respective parental lines as shown in Supplemental Table S13. Homozygous lines were identified by genotyping using the corresponding genotyping primers in Supplemental Table S14. In case of fluorophor-fusion lines, the offspring of a potential homozygous plant was checked for fluorescence signals to verify homozygosity. CRISPR/Cas9 deletion mutants were additionally selected according to the loss of the CRISPR/Cas9 construct in the following generation. All newly established Arabidopsis lines are homozygous, except two of the crossing lines as stated in Supplemental Table S13.

Confocal Microscopy

Live cell imaging, except for rBiFC assays, was performed with a Zeiss LSM880, AxioObserver SP7 confocal laser-scanning microscope, equipped with either a Zeiss C-Apochromat 40×/1.2 W AutoCorr M27 water-immersion objective or a Plan-Apochromat 20x/0.8 M27 objective (INST 248/254-1). Vacuole stainings were carried out as described previously (Scheuring et al., 2015). Cell walls were stained by mounting roots in 0.01 mg/ml PI solution. Fluorescence signals were acquired for mTurquoise (excitation/emission 405 nm/464-482 nm), MDY-64 (excitation/emission 458 nm/473–527 nm), GFP and BCECF (excitation/emission 488 nm/500–571 nm), RFP/mCherry (excitation/emission 594 nm/598–

687 nm), FM4-64 (excitation/emission 543 nm/583–758 nm) and PI (excitation/emission 543 nm/580–718 nm), and processed using Zeiss software ZEN 2.3 or Fiji software (https://imagej.net/Fiji). Z-stacks were recorded with a step size of either 400 nm (for quantitative analysis of actin filament organization) or 540 nm (for 3D reconstruction of cells and vacuoles and assessment of vacuolar occupancy). For rBiFC experiments, samples were imaged using the Leica TCS SP8 WLL SMD-FLIM-FCS with an HC PL APO CS2 63x/1.20 (water) objective. Fluorophores were excited using a white laser (514 nm for YFP, 570 nm for RFP) and the emission was detected using hybrid detectors (HyD SMD; 520-560 nm for YFP, 580-630 nm for RFP).

Phenotype Analysis

Root length, calculation of vacuolar morphology index (vac. morph. index,VMI), plasma membrane-tonoplast distance and vacuolar occupancy of the cell (occupancy) were carried out as described previously (Kaiser et al., 2019). For the quantification of vacuolar structures (VS), epidermis cells from the late meristem were used to count seemingly disconnected structures based on single subcortical confocal images. VMI measurements of *amiR-vps16* and NET4A-GFP^{OE} x *amiR-vps16* were conducted in the early elongation zone, taken into account cells that were twice as long as wide. To assess differences in root waviness, root straightness was analyzed as an indirect representation. Therefore, the standard root length (L), in which the extra length due to root waves is included, was measured as usual. In addition, the vertical root length (Lv) was measured as a straight line from root tip to collet start (Fig 2E) and root straightness indicated as the Lv/L ratio.

Quantification of actin filament organization

To investigate the actin filament organization, z-stacks of root epidermal cells were acquired for the late meristematic/early elongated zone. For quantitative analysis, z-stack recordings were processed to half z-stacks, covering early elongated cells of atrichoblast files from the outer cortical confocal section to the cell center (at the position of the nucleus), and used to create maximum intensity projections. Parallelness of actin filaments was then quantified for a defined rectangular area (24.39x11.62 µm) within a single early elongated atrichoblast cell (excluding cell borders) on each maximum intensity projection using the LPX plugin for ImageJ (URL: https://lpixel.net/services/research/lpixel-imagej-plugins/) according to Higaki (Higaki, 2017). Briefly, a box outlining the defined area of a cell used for quantification was created using the “rectangle” tool of the toolbar menu and added as ROI to the ROI manager. Actin filaments were skeletonized using the “Lpx Filter2d” plugin with “lineFilters” set as filter and “lineExtract” set as linemode. The parameters for “lineExtract” were set to giwsiter = 5, mdnmsLen = 15, pickup = otsu, shaveLen = 5 and delLen = 5. To exclude skeletonized actin filaments outside the desired area of the image, they were masked by inverting the previously created ROI (“Edit→Selection→Make Inverse”) and painting it black using “Edit→Fill” while the intensity value of the “Color picker” tool from the toolbar menu is set to zero. The “Lpx Filter2d” plugin was then used on this masked image with “lineFilters” set as filter and “lineFeature” set as linemode to eventually calculate parallelness (given as “a_normAvgRad” value).

3D Surface Rendering

3D reconstruction of cells and vacuoles was performed using Imaris 8.4 (Bitplane) software (https://imaris.oxinst.com/). For the creation of cell models, the manual drawing function (distance) of the surface creation tool was used. Cell borders were marked according to the signals for PI channel on at least every third slice of a z-stack. Subsequently, a surface representing the whole cell was created based on these markings. The surface was then used to produce a masked version of the BCECF-AM channel by using the mask selection function in the edit menu and setting the voxels outside the surface to 0. For the creation of the vacuole models, this masked channel was used to automatically create a second surface corresponding to the BCECF signals. Before completing the surface rendering, the displayed model was visually compared to the underlying BCECF signals and adjustments were made using the absolute intensity threshold option. Eventually, the volumes of the generated 3D models, each given in the statistic menu of the respective surface, were used to calculate the vacuolar occupancy of the cell.

Protein extraction

Arabidopsis proteins, excect for Co-immunoprecipitation, were extracted from 8 days old seedlings' roots. Frozen material was grinded in liquid nitrogen and the powder resuspended in four times of its amount of extraction buffer (100 mM KCl, 20 mM 4-(2-hydroxyethyl)-1-piperazineethanesulfonic acid (HEPES), 2 mM Dithiothreitol (DTT), 1 mM phenylmethylsulfonyl fluoride (PMSF), 0.1 mM ethylenediaminetetraacetic acid (EDTA) and 1x cOmplete™, EDTA-free Protease Inhibitor Cocktail (Roche, Switzerland); pH 7.5). The supernatant after centrifugation was used to determine protein concentration via Pierce assay and equal amounts of samples were further processed for immunological detections. For *N. benthamina* leaf samples from rBIFC experiments, protein extraction was performed using Lyse and Load (LL-) buffer (50 mM Tris/HCl; pH 6.8, including 2 % sodium dodecylsulfate (SDS), 7 M urea, 30 % glycerol, 0.1 M DTT and 0.04 % bromphenol blue. Proteins of cell culture samples from mbSUS assays were extracted using the same LL-buffer according to Asseck and Grefen (Asseck and Grefen, 2018).

Immunological detection

For immunological detection, samples were separated via sodium dodecylsulfate polyacrylamide gel electrophoresis (SDS–PAGE). If necessary, samples were mixed with loading dye, incubated at 95 °C for 5 min and shortly centrifuged prior to loading. Blotting was performed using either a nitrocellulose (GE Healthcare, USA) or a polyvinylidene difluoride (PVDF) membrane (Sigma-Aldrich). Membranes were blocked with 5 % skim milk powder in TBS-T (150 mM NaCl, 10 mM Tris/HCl pH 8.0, 0.1% Tween 20), washed with TBS-T and then incubated with the first antibody solution. After washing the membrane again, it was probed with the second antibody for 1 h. Subsequently, the membrane was washed another three times at least, submerged with ECL solution (ECL Prime Kit; Amersham, UK) and chemiluminescence signals were detected using the ChemiDoc system from BioRad. The following antibodies were used: monoclonal anti GFP antibody (1:500; Roche), monoclonal anti HA antibody (1:1000, Roche), polyclonal anti VP16 antibody (Genetex; 1:1000), polyclonal anti NET4 (1:10000) and monoclonal anti HIS antibody (1:3000; Thermo-Fisher).

Co-Immunoprecipitation and mass spectrometry

For the co-immunoprecipitation, 7-day-old seedlings (Col-0, NET4A-GFP, NET4A-GFP^{OE}) were grown on plates. From every plate, 500 mg plant material was harvested, frozen and grinded in liquid nitrogen. Four individual replicates were carried out. 1.5 ml extraction buffer (50 mM NaCl, 50 mM HEPES pH 8, 5 mM $MgCl_2$, 1 mM PMSF, 2 mM DSP (crosslinker) and 1x cOmplete^{TM}, EDTA-free Protease Inhibitor) was added and the samples incubated for 30 min at 4°C. After quenching, lysates were clarified by centrifugation twice at 16,000 g at 4°C. Supernatant was applied onto GFP-nanobodies coupled to magnetic agarose beads (GFP-trap, ChromoTek, Germany) equilibrated in lysis buffer. Beads were incubated with the lysate on an end over end shaker for 1 h at 4°C. To wash the beads, tubes were magnetized for 1 min, the supernatant discarded and 750 µl wash-buffer (50 mM NaCl, 50 mM Tris-HCL pH 8.0, 0.05% Tween-20; 5 mM $MgCl_2$) was added and tubes were agitated on an end over end shaker for 1 min at 4°C. Two wash cycles were done, followed by three in wash-buffer lacking Tween-20. The final bead pellet was resuspended in 100 µl 2xSDS sample buffer (120 mM Tris-HCL pH 6.8, 20% glycerol, 4% SDS, 0.04 bromphenol blue, 100 mM DTT) and boiled for 1 min at 98°C. After magnetizing again, the eluate was transferred into a new tube and 20 µl were loaded on a 10% SDS-PAGE. Samples were run for approximately 1.5 cm into the separating gel, gels were stained with colloidal Coomassie for 3 h. Visible protein bands were cut out and destained for 30 s using destaining solution (10 % acetic acid, 25 % methanol). Before and after cutting, pictures were taken for documentation purposes. After destaining, the cut bands were diced into 1 x 1 mm cubes and transferred into a reaction tube filled with 0.5 ml of 25 % methanol. The prepared samples were then further processed and analyzed by mass spectrometry as described previously (Müller et al., 2018). After analysis, the raw data were processed with MaxQuant (1.6.3.3) using the latest Uniprot Arabidopsis proteome fasta file. Statistical data analysis was performed using Perseus (Tyanova et al., 2016). First, protein LFQ-values were Log_2-transformed and accessions were removed that were identified in less than two replicates in one of the two categories (Col-0, NET4A-GFP^{OE}). For statistics, missing values were imputed, based on all measured log2 LFQ intensities, with random numbers. Enrichment between NET4A-GFP^{OE} and Col-0 was determined by one-sided *t*-test and permutation-based FDR of 0.05 and S_0 = 1 (when both compared sample sets contained at least three valid values).

Recombinant protein expression and antibody generation

Recombinant protein expression of NET4A in *E. coli* strain was carried out as previously described (Jeblick et al., 2023). The antibody against NET4A was raised by immunizing rabbits with the full-length protein.

Protein-Lipid overlay assay

Lipid overlay assays, using P-6001 PIP stripes (Echelon Biosciences) were performed according to the manufacturer's instructions.

Ratiometric Bimolecular Fluorescence Complementation (rBiFC)

Agrobacterium-mediated transient transformation of approximately 4-week old *N. benthamiana* leaves with 2in1 rBiFC constructs was performed as described previously (Mehlhorn et al., 2018). Fluorescence intensities were recorded 2 days' post infiltration for approximately 20-30 images per construct. Ratios between complemented YFP fluorescence and RFP were calculated and plotted using Fiji and Graphpad Prism5 software.

Immunoblotting verified protein expression utilizing anti NET4A antibody and anti HA peroxidase conjugated antibody, respectively.

Mating-based split ubiquitin system (mbSUS)

Bait/Cub fusions and prey/Nub fusions were generated by cloning the desired genes of interest into the Gateway-compatible vectors pMetOYC-Dest and pNX35-Dest, respectively. These were transformed into haploid yeast strains THY.AP4 (Cub fusion) and THY.AP5 (Nub fusions) as described previously (Asseck and Grefen, 2018). After mating, diploid yeasts were dropped in 10 times OD dilutions on growth control (CSM-Leu-, Trp-, Ura-) and interaction-selective media (CSM-Leu-, Trp-, Ura-, Ade-, His-) supplemented with 50 or 500 µM methionine. The non-mutated N-terminal ubiquitin moiety (NubI) was used as positive control, and NubI13G (NubG) as negative control. Protein expression was verified in haploid yeast using antibodies against the VP16 domain for the Cub fusion or the HA epitope tag for the Nub fusions.

Transient gene expression

Transient expression was performed as previously described (Jeblick et al., 2023). Infiltrated areas were marked for easier identification and plants were incubated under reduced light conditions for 48-72 h prior microscopic analysis.

GUS-staining

GUS staining of NET4A::GUS-GFP and NET4B::GUS-GFP seedlings was performed as described elsewhere (Béziat et al., 2017). Samples were recorded using a Leica MZ125 stereomicroscope or a Zeiss Observer A.1 microscope with a Leica DMC 4500 camera attached.

Gene Accession Codes

Sequence data of gene and protein sequences used in this article can be found at the Arabidopsis Information Resource (TAIR; http://www.arabidopsis.org/), GenBank/EMBL, Aramemnon (http://aramemnon.uni-koeln.de/), or UniProt (https://www.uniprot.org/proteomes/UP000006548databases) under the following accession numbers: NET4A (At5g58320), NET4B (At2g30500), NET3A (At1g03470), NET3C (At2g47920), RABG3A (At4g09720), RABG3B (At1g22740, VPS16 (At2g38020), VAMP711 (At4g32150), RABC1 (At1g43890) and VAP27-1 (At3g60600).

Statistical analysis

All quantitative data was analyzed using the GraphPad Prism 5 or 9 software (https://www.graphpad.com/scientific-software/prism/). The precise statistical method used is given in the respective figure legends. Box-plot borders in the graphs represent 25th to 75th percentile, the horizontal line the median and whiskers minimum to maximum values.

Supplemental data

Supplementary Figure S1. NET4B functions similar to NET4A.

Supplementary Figure S2. NET4A overexpression leads to actin bundling from the cell periphery to the nucleus.

Supplementary Figure S3. Crossing of *net4a net4b* and NET4A-GFP^{OE} complements vacuolar phenotypes.

Supplementary Figure S4. NET4A overexpression stabilizes actin filaments.
Supplementary Figure S5. *rabg3a,b,c,d,e,f* sextuple and *rabg3a,b,c,d,e,f net4a* septuple mutants show more round vacuoles and inhibited root growth.
Supplementary Figure S6. Confirmation of NET4A interaction.
Supplementary Figure S7. Lipid overlay assays (PIP-strips) using NET4 protein.
Supplementary Figure S8. Expression control for mbSUS experiments in Fig 6.
Supplementary Figure S9. NET4A and NET4B both show localization at the nuclear envelope.
Supplementary Figure S10. *NET4A* and *NET4B* gene expression in Arabidopsis using promoter-GUS fusions.
Supplementary Figure S11. *NET4A* and *NET4B* expression using promoter-GFP fusions.
Supplementary Figure S12. Phenotypic characterization of *net3a* and *net4a net4b net3a* mutants.
Supplementary Figure S13. Schematic overview of CRISPR/Cas9 derived deletions for *NET4A*, *NET4B*, *NET3A* and *NET3C*.
Supplemental Table S1: Primers used for qRT-PCR.
Supplemental Table S2: List of used expression constructs generated by GreenGate cloning.
Supplemental Table S3: Primers used for GreenGate cloning.
Supplemental Table S4: List of entry vectors used for GreenGate cloning.
Supplemental Table S5: Primers for amplification of *amiR-vps16* sequence.
Supplemental Table S6: Primers used to generate pHEE-mCherry.
Supplemental Table S7: Primers used for the generation of CRISPR/Cas9 constructs.
Supplemental Table S8: List of used CRISPR/Cas9 constructs for generating deletion mutants.
Supplemental Table S9: List of CRISPR/Cas9 derived deletion mutants.
Supplemental Table S10: Primers used for the generation of rBiFC and mbSUS constructs.
Supplemental Table S11: List of generated Gateway expression constructs used for rBiFC and mbSUS experiments.
Supplemental Table S12: Primers used to clone constructs for recombinant protein expression.
Supplemental Table S13: List of Arabidopsis lines obtained by crossing.
Supplemental Table S14: Primers used for genotyping.

Acknowledgements

We would like to thank Takashi Ueda for providing the *rabg3a,b,c,d,e,f* sextuple mutant and Joe McKenna for the RFP-HDEL Arabidopsis line and plasmid. We thank Matthias Hahn for critical reading of the manuscript and constructive advice throughout the project. Technical help from Patrick Pattar, Anne Lau, Sophie Eisele and Benjamin Ziehmer is highly appreciated. For the kind willingness to share facilities and equipment, we thank Ekkehard Neuhaus. This work was supported by grants from the *BioComp* research initiative (Rhineland-Palatinate, Germany) and the German research foundation (DFG; SCHE 1836/4-1 and SCHE 1836/4-2) to D.S.

Literature

Aniento, F., Sánchez de Medina Hernández, V., Dagdas, Y., Rojas-Pierce, M., and Russinova, E. (2022). Molecular mechanisms of endomembrane trafficking in plants. The Plant Cell **34** (1): 146–173.

Asseck, L.Y., and Grefen, C. (2018). Detecting Interactions of Membrane Proteins: The Split-Ubiquitin System. Methods in molecular biology (Clifton, N.J.) **1794**: 49–60.

Balderhaar, H.J.k., and Ungermann, C. (2013). CORVET and HOPS tethering complexes - coordinators of endosome and lysosome fusion. Journal of cell science **126** (Pt 6): 1307–1316.

Brillada, C., Zheng, J., Krüger, F., Rovira-Diaz, E., Askani, J.C., Schumacher, K., and Rojas-Pierce, M. (2018). Phosphoinositides control the localization of HOPS subunit VPS41, which together with VPS33 mediates vacuole fusion in plants. Proceedings of the National Academy of Sciences of the United States of America **115** (35): E8305-E8314.

Chytilova, E., Macas, J., Sliwinska, E., Rafelski, S.M., Lambert, G.M., and Galbraith, D.W. (2000). Nuclear dynamics in Arabidopsis thaliana. Molecular Biology of the Cell **11** (8): 2733–2741.

Cui, Y., Zhao, Q., Hu, S., and Jiang, L. (2020). Vacuole Biogenesis in Plants: How Many Vacuoles, How Many Models? Trends in plant science **25** (6): 538–548.

Deeks, M.J., Calcutt, J.R., Ingle, E.K.S., Hawkins, T.J., Chapman, S., Richardson, A.C., Mentlak, D.A., Dixon, M.R., Cartwright, F., Smertenko, A.P., Oparka, K., and Hussey, P.J. (2012). A superfamily of actin-binding proteins at the actin-membrane nexus of higher plants. Current biology CB **22** (17): 1595–1600.

Duckney, P.J., Wang, P., and Hussey, P.J. (2022). Membrane contact sites and cytoskeleton-membrane interactions in autophagy. FEBS letters **596** (17): 2093–2103.

Ebine, K., Inoue, T., Ito, J., Ito, E., Uemura, T., Goh, T., Abe, H., Sato, K., Nakano, A., and Ueda, T. (2014). Plant vacuolar trafficking occurs through distinctly regulated pathways. Current biology CB **24** (12): 1375–1382.

Eitzen, G., Wang, L., Thorngren, N., and Wickner, W. (2002). Remodeling of organelle-bound actin is required for yeast vacuole fusion. The Journal of cell biology **158** (4): 669–679.

Ge, S., Zhang, R.-X., Wang, Y.-F., Sun, P., Chu, J., Li, J., Sun, P., Wang, J., Hetherington, A.M., and Liang, Y.-K. (2022). The Arabidopsis Rab protein RABC1 affects stomatal development by regulating lipid droplet dynamics. The Plant Cell **34** (11): 4274–4292.

Geldner, N., Dénervaud-Tendon, V., Hyman, D.L., Mayer, U., Stierhof, Y.-D., and Chory, J. (2009). Rapid, combinatorial analysis of membrane compartments in intact plants with a multicolor marker set. The Plant journal for cell and molecular biology **59** (1): 169–178.

Gilliland, L.U., Pawloski, L.C., Kandasamy, M.K., and Meagher, R.B. (2003). Arabidopsis actin gene ACT7 plays an essential role in germination and root growth. The Plant journal for cell and molecular biology **33** (2): 319–328.

Grefen, C., Obrdlik, P., and Harter, K. (2009). The determination of protein-protein interactions by the mating-based split-ubiquitin system (mbSUS). Methods in molecular biology (Clifton, N.J.) **479**: 217–233.

Gundersen, G.G., and Worman, H.J. (2013). Nuclear positioning. Cell **152** (6): 1376–1389.

Hawkins, T.J., Kopischke, M., Duckney, P.J., Rybak, K., Mentlak, D.A., Kroon, J.T.M., Bui, M.T., Richardson, A.C., Casey, M., Alexander, A., Jaeger, G. de, **Kalde, M., Moore, I., Dagdas, Y., Hussey, P.J., and Robatzek, S.** (2023). NET4 and RabG3 link actin to the tonoplast and facilitate cytoskeletal remodelling during stomatal immunity. Nature Communications **14** (1): 5848.

Higaki, T. (2017). Quantitative evaluation of cytoskeletal organizations by microscopic image analysis. PLANT MORPHOL **29** (1): 15–21.

Jeblick, T., Leisen, T., Steidele, C.E., Albert, I., Müller, J., Kaiser, S., Mahler, F., Sommer, F., Keller, S., Hückelhoven, R., Hahn, M., and Scheuring, D. (2023). Botrytis hypersensitive response inducing protein 1 triggers noncanonical PTI to induce plant cell death. Plant Physiology **191** (1): 125–141.

Kaiser, S., Eisa, A., Kleine-Vehn, J., and Scheuring, D. (2019). NET4 Modulates the Compactness of Vacuoles in Arabidopsis thaliana. International journal of molecular sciences **20** (19).

Kaiser, S., Eisele, S., and Scheuring, D. (2021). Vacuolar occupancy is crucial for cell elongation and growth regardless of the underlying mechanism. Plant Signaling & Behavior **16** (8): 1922796.

Kaiser, S., and Scheuring, D. (2020). To Lead or to Follow: Contribution of the Plant Vacuole to Cell Growth. Frontiers in Plant Science **11**: 553.

Kandasamy, M.K., McKinney, E.C., and Meagher, R.B. (2009). A single vegetative actin isovariant overexpressed under the control of multiple regulatory sequences is sufficient for normal Arabidopsis development. The Plant Cell **21** (3): 701–718.

Ketelaar, T., Faivre-Moskalenko, C., Esseling, J.J., Ruijter, N.C.A. de, **Grierson, C.S., Dogterom, M., and Emons, A.M.C.** (2002). Positioning of nuclei in Arabidopsis root hairs: an actin-regulated process of tip growth. The Plant Cell **14** (11): 2941–2955.

Kost, B., and Chua, N.-H. (2002). The plant cytoskeleton: vacuoles and cell walls make the difference. Cell **108** (1): 9–12.

Labun, K., Montague, T.G., Gagnon, J.A., Thyme, S.B., and Valen, E. (2016). CHOPCHOP v2: a web tool for the next generation of CRISPR genome engineering. Nucleic Acids Research **44** (W1): W272-6.

Lampropoulos, A., Sutikovic, Z., Wenzl, C., Maegele, I., Lohmann, J.U., and Forner, J. (2013). GreenGate - A Novel, Versatile, and Efficient Cloning System for Plant Transgenesis. PLOS ONE **8** (12).

Lupanga, U., Röhrich, R., Askani, J., Hilmer, S., Kiefer, C., Krebs, M., Kanazawa, T., Ueda, T., and Schumacher, K. (2020). The Arabidopsis V-ATPase is localized to the TGN/EE via a seed plant-specific motif. eLife **9**.

McDowell, J.M., An, Y.Q., Huang, S., McKinney, E.C., and Meagher, R.B. (1996). The arabidopsis ACT7 actin gene is expressed in rapidly developing tissues and responds to several external stimuli. Plant Physiology **111** (3): 699–711.

Mehlhorn, D.G., Wallmeroth, N., Berendzen, K.W., and Grefen, C. (2018). 2in1 Vectors Improve In Planta BiFC and FRET Analyses. Methods in molecular biology (Clifton, N.J.) **1691**: 139–158.

Minina, E.A., Scheuring, D., Askani, J., Krueger, F., and Schumacher, K. (2021). Light at the end of the tunnel: FRAP assay reveals that plant vacuoles start as a tubular network. bioRxiv **10.1101/2021.05.13.444058**.

Müller, N., Leroch, M., Schumacher, J., Zimmer, D., Könnel, A., Klug, K., Leisen, T., Scheuring, D., Sommer, F., Mühlhaus, T., Schroda, M., and Hahn, M. (2018). Investigations on VELVET regulatory mutants confirm the role of host tissue acidification and secretion of proteins in the pathogenesis of Botrytis cinerea. The New phytologist **219** (3): 1062–1074.

Narusaka, M., Shiraishi, T., Iwabuchi, M., and Narusaka, Y. (2010). The floral inoculating protocol: a simplified Arabidopsis thaliana transformation method modified from floral dipping. Plant Biotechnology **27** (4): 349–351.

Noack, L.C., and Jaillais, Y. (2017). Precision targeting by phosphoinositides: how PIs direct endomembrane trafficking in plants. Current opinion in plant biology **40**: 22–33.

Peremyslov, V.V., Prokhnevsky, A.I., and Dolja, V.V. (2010). Class XI myosins are required for development, cell expansion, and F-Actin organization in Arabidopsis. The Plant Cell **22** (6): 1883–1897.

Pfaffl, M.W. (2001). A new mathematical model for relative quantification in real-time RT-PCR. Nucleic Acids Research **29** (9): e45.

Riedl, J., Crevenna, A.H., Kessenbrock, K., Yu, J.H., Neukirchen, D., Bista, M., Bradke, F., Jenne, D., Holak, T.A., Werb, Z., Sixt, M., and Wedlich-Soldner, R. (2008). Lifeact: a versatile marker to visualize F-actin. Nature Methods **5** (7): 605–607.

Rojo, E., Gillmor, C.S., Kovaleva, V., Somerville, C.R., and Raikhel, N.V. (2001). VACUOLELESS1 is an essential gene required for vacuole formation and morphogenesis in Arabidopsis. Developmental cell **1** (2): 303–310.

Rosero, A., Oulehlová, D., Stillerová, L., Schiebertová, P., Grunt, M., Žárský, V., and Cvrčková, F. (2016). Arabidopsis FH1 Formin Affects Cotyledon Pavement Cell Shape by Modulating Cytoskeleton Dynamics. Plant & cell physiology **57** (3): 488–504.

Scheuring, D., Löfke, C., Krüger, F., Kittelmann, M., Eisa, A., Hughes, L., Smith, R.S., Hawes, C., Schumacher, K., and Kleine-Vehn, J. (2016). Actin-dependent vacuolar occupancy of the cell determines auxin-induced growth repression. Proceedings of the National Academy of Sciences of the United States of America **113** (2): 452–457.

Scheuring, D., Schöller, M., Kleine-Vehn, J., and Löfke, C. (2015). Vacuolar staining methods in plant cells. Methods in molecular biology (Clifton, N.J.) **1242**: 83–92.

Scorrano, L., Matteis, M.A. de, **Emr, S., Giordano, F., Hajnóczky, G., Kornmann, B., Lackner, L.L., Levine, T.P., Pellegrini, L., Reinisch, K., Rizzuto, R., Simmen, T., Stenmark, H., Ungermann, C., and Schuldiner, M.** (2019). Coming together to define membrane contact sites. Nature Communications **10**.

Shvarev, D., Schoppe, J., König, C., Perz, A., Füllbrunn, N., Kiontke, S., Langemeyer, L., Januliene, D., Schnelle, K., Kümmel, D., Fröhlich, F., Moeller, A., and Ungermann, C. (2022). Structure of the HOPS tethering complex, a lysosomal membrane fusion machinery. eLife **11**.

Starr, M.L., and Fratti, R.A. (2019). The Participation of Regulatory Lipids in Vacuole Homotypic Fusion. Trends in biochemical sciences **44** (6): 546–554.

Stemmer, M., Thumberger, T., Del Sol Keyer, M., Wittbrodt, J., and Mateo, J.L. (2015). CCTop: An Intuitive, Flexible and Reliable CRISPR/Cas9 Target Prediction Tool. PLOS ONE **10** (4): e0124633.

Stephani, M., Picchianti, L., Gajic, A., Beveridge, R., Skarwan, E., Sanchez de Medina Hernandez, V., Mohseni, A., Clavel, M., Zeng, Y., Naumann, C., Matuszkiewicz, M., Turco, E., Loefke, C., Li, B., Dürnberger, G., Schutzbier, M., Chen, H.T.,

Abdrakhmanov, A., Savova, A., Chia, K.-S., Djamei, A., Schaffner, I., Abel, S., Jiang, L., Mechtler, K., Ikeda, F., Martens, S., Clausen, T., and Dagdas, Y. (2020). A cross-kingdom conserved ER-phagy receptor maintains endoplasmic reticulum homeostasis during stress. eLife **9**.

Stührwohldt, N., Scholl, S., Lang, L., Katzenberger, J., Schumacher, K., and Schaller, A. (2020). The biogenesis of CLEL peptides involves several processing events in consecutive compartments of the secretory pathway. eLife **9**.

Takemoto, K., Ebine, K., Askani, J.C., Krüger, F., Gonzalez, Z.A., Ito, E., Goh, T., Schumacher, K., Nakano, A., and Ueda, T. (2018). Distinct sets of tethering complexes, SNARE complexes, and Rab GTPases mediate membrane fusion at the vacuole in Arabidopsis. Proceedings of the National Academy of Sciences of the United States of America **115** (10): E2457-E2466.

Tan, J.X., and Finkel, T. (2022). A phosphoinositide signalling pathway mediates rapid lysosomal repair. Nature **609** (7928): 815–821.

Tyanova, S., Temu, T., and Cox, J. (2016). The MaxQuant computational platform for mass spectrometry-based shotgun proteomics. Nature protocols **11** (12): 2301–2319.

Vale, R.D. (2003). The molecular motor toolbox for intracellular transport. Cell **112** (4): 467–480.

Viotti, C., Krüger, F., Krebs, M., Neubert, C., Fink, F., Lupanga, U., Scheuring, D., Boutté, Y., Frescatada-Rosa, M., Wolfenstetter, S., Sauer, N., Hillmer, S., Grebe, M., and Schumacher, K. (2013). The endoplasmic reticulum is the main membrane source for biogenesis of the lytic vacuole in Arabidopsis. The Plant Cell **25** (9): 3434–3449.

Waadt, R., Krebs, M., Kudla, J., and Schumacher, K. (2017). Multiparameter imaging of calcium and abscisic acid and high-resolution quantitative calcium measurements using R-GECO1-mTurquoise in Arabidopsis. New Phytol **216** (1): 303–320.

Wang, P., Duckney, P., Gao, E., Hussey, P.J., Kriechbaumer, V., Li, C., Zang, J., and Zhang, T. (2023). Keep in contact: multiple roles of endoplasmic reticulum-membrane contact sites and the organelle interaction network in plants. New Phytol **238** (2): 482–499.

Wang, P., Hawkins, T.J., Richardson, C., Cummins, I., Deeks, M.J., Sparkes, I., Hawes, C., and Hussey, P.J. (2014). The plant cytoskeleton, NET3C, and VAP27 mediate the link between the plasma membrane and endoplasmic reticulum. Current biology CB **24** (12): 1397–1405.

Wang, Z.-P., Xing, H.-L., Dong, L., Zhang, H.-Y., Han, C.-Y., Wang, X.-C., and Chen, Q.-J. (2015). Egg cell-specific promoter-controlled CRISPR/Cas9 efficiently generates homozygous mutants for multiple target genes in Arabidopsis in a single generation. Genome biology **16** (1): 144.

Wickner, W. (2010). Membrane fusion: five lipids, four SNAREs, three chaperones, two nucleotides, and a Rab, all dancing in a ring on yeast vacuoles. Annual review of cell and developmental biology **26**: 115–136.

Xing, H.-L., Dong, L., Wang, Z.-P., Zhang, H.-Y., Han, C.-Y., Liu, B., Wang, X.-C., and Chen, Q.-J. (2014). A CRISPR/Cas9 toolkit for multiplex genome editing in plants. BMC plant biology **14**: 327.

Zang, J., Klemm, S., Pain, C., Duckney, P., Bao, Z., Stamm, G., Kriechbaumer, V., Bürstenbinder, K., Hussey, P.J., and Wang, P. (2021). A novel plant actin-microtubule

bridging complex regulates cytoskeletal and ER structure at ER-PM contact sites. Current biology CB **31** (6): 1251-1260.e4.